

Optimized Perovskite Electrocatalyst for Bifunctional Air Electrode by Impedance Spectroscopy Analysis

Shuxin Zhuang¹, Houan Zhang^{1,*}, Suqin Liu², Feiyue Tu², Wenxian Zhang¹, Chunzhao Zhao¹

¹ School of Materials Science and Engineering, Xiamen University of Technology, Xiamen, 361024, China

² College of Chemistry and Chemical Engineering, Central South University, Changsha, 410083, China

*E-mail: zsxtony@xmut.edu.cn

Received: 25 November 2013 / Accepted: 7 January 2014 / Published: 2 February 2014

Perovskite $\text{La}_{0.6}\text{Ca}_{0.4}\text{CoO}_3$ is a promising cathode catalyst for the application in metal-air batteries as it shows good stability during cycling. However, its poor electrical conductivity increases the polarization loss and low specific surface area reduces the catalytic activity. In order to optimize its catalytic activity, well-dispersed nanoporous $\text{La}_{0.6}\text{Ca}_{0.4}\text{CoO}_3$ are prepared by a modified amorphous citrate precursor method. The activities are investigated using electrochemical impedance spectroscopy (EIS). The impedance spectra are analyzed by an equivalent circuit containing an electrode intrinsic resistance at the high frequency and kinetic impedance through the porous electrode at the low frequency. The EIS results confirm that the nanoporous $\text{La}_{0.6}\text{Ca}_{0.4}\text{CoO}_3$ with high specific surface area could decrease both intrinsic and kinetic impedance, indicating that they have the higher electrical conductivity and electrocatalytic activity than the common $\text{La}_{0.6}\text{Ca}_{0.4}\text{CoO}_3$ catalyst.

Keywords: Electrocatalyst; Perovskite; Electrochemical impedance spectroscopy

1. INTRODUCTION

Electrically rechargeable metal-air batteries are promising power sources because they have high specific energy and are inexpensive and environmentally benign [1-8]. However, potential for improvement remains with respect to a longer cycle life and higher power-drain capability of the metal-air battery. The characteristics of metal-air battery mainly depend on the activity and stability of the gas-diffusion electrodes (GDEs) where oxygen reduction (ORR) and evolution (OER) reaction occurred. For these electrodes, carbon materials are promising substrates, because they provide a high surface area for catalyst dispersion and exhibit a good activity in alkaline media for oxygen reduction

to peroxide ions [9-11]. For economic reasons, perovskites [12-13], spinels [14-15], and pyrochlores [16-17] have become interesting alternative catalysts to noble metals. Among these catalysts, perovskite-type $\text{La}_{0.6}\text{Ca}_{0.4}\text{CoO}_3$ has drawn much attention due to its relatively good stability and catalytic activity [18-21]. The activity of this catalyst mainly resides in its ability to decompose the hydrogen peroxide produced by oxygen reduction on the carbon support [22-23]. The active materials (carbon and catalyst) are typically bonded with tetrafluoroethylene (PTFE) into porous gas-diffusion electrodes (GDEs).

For a bifunctional air electrode with high activity and stability, the selection of catalyst and substrate material, the mixing ratio and preparation of active catalysts as well as the hydrophobicity and hydrophilicity of the electrode need to be optimized. Among these influencing factors, optimization of active catalysts for oxygen reduction reaction has become a focus in recent years [24-27]. However, there is no intuitionistic technique to characterize the effect of catalysts on the performance of GDEs. EIS has been proven to be a powerful and useful tool for the characterization of electrochemical systems [28-30]. In combination with Brunauer-Emmett-Teller (BET) analysis, scanning electron microscopy (SEM) and energy dispersive X-ray (EDS) analysis, it will provide important guides for the optimization of the active catalysts for GDEs.

It was a major goal of this study to use EIS to characterize the GDEs with various catalysts prepared by our group, and attempt to separate electronic resistances from the mass-transport processes taking place at the porous electrode. GDEs containing various catalysts with different surface areas were first tested by EIS in oxygen reduction under different overpotentials. The impedance spectra obtained were fitted with a simplified equivalent circuit containing just four parameters accounting for the intrinsic resistance of porous electrode (R_1), the resistance of charge-transfer processes at the catalyst surface or reacting species diffusion through the thin film (R_2) and the two double-layer capacitances (CPE_1 and CPE_2).

2. EXPERIMENTAL

2.1 Optimization of catalyst powders

The nanoporous catalyst $\text{La}_{0.6}\text{Ca}_{0.4}\text{CoO}_3$ powder was synthesized by a modified amorphous citrate precursor (ACP) method [31]. Carbon black (Vulcan XC-72R, 30 nm, Cabot) was used as a pore-forming material. $\text{La}(\text{NO}_3)_3 \cdot 6\text{H}_2\text{O}$, $\text{Ca}(\text{NO}_3)_2 \cdot 4\text{H}_2\text{O}$, $\text{Co}(\text{NO}_3)_3 \cdot 6\text{H}_2\text{O}$ and citric acid were used as reagents. An aqueous solution of citric acid with a 10% excess over the number of ionic equivalents of cations was prepared. The aqueous solution of citric acid was added to various amounts of pore former material, in which the weight ratio of pore former to the theoretical mass of $\text{La}_{0.6}\text{Ca}_{0.4}\text{CoO}_3$ were 0:1, 1:1, 2:1 and 3:1, labeled as the ACP-derived LCCO, LCCO-1, LCCO-2 and LCCO-3, respectively. Then they were agitated vigorously for 4 h in room temperature. Subsequently, the aqueous solutions of the stoichiometric metal nitrates were gradually added to the as-prepared solution and they were agitated for another 15 min. The resulting solution was concentrated by slowly evaporating water under vacuum in a rotavapor at 75 °C until a gel was obtained. This gel was dried in an oven, in which

temperature slowly increased to 200 °C and was kept for about 12 h to produce a solid amorphous citrate precursor. The precursor was milled and calcined in air at 650 °C for 4 h, respectively.

Phase identifications of the synthesized powders were conducted by a MXPAHF X-ray diffractometer from 20 ° to 80 ° with a Cu K α of 1.54056 Å. Both the morphologies and EDS of the synthesized powders were observed by a JSM–SEM 6360. Specific surface area was measured by nitrogen adsorption-desorption with the BET method.

2.2 Electrode preparation and electrochemical measurement

The manufacturing process for the electrodes is described as below. To prepare the semi-hydrophobic catalytic layer of the GDE, 25 wt.% catalyst powder and 50 wt.% carbon black (Vulcan XC-72R) were ball-milled in excess 2-propanol/H₂O (1:1) for 30 min, and then 25 wt.% diluted polytetrafluorethylene suspension (10 wt.% PTFE in H₂O) and proper quantities of acetone were added to the catalyst/Vulcan XC-72R mixture. In the presence of acetone, a very homogeneous dispersion of Teflon on a substrate was observed. This mixture was blended for 30 min with ultrasonic agitation and then dried at 80 °C to give a dough-like paste, which was finally rolled into a thin layer of about 200 μm thickness and the catalyst loading was approximately kept at 2.0 mg cm⁻². A hydrophobic gas diffusion layer containing only acetylene black and PTFE with weight ratios of 7:3 was prepared by the same process. The catalytic layer and a gas diffusion layer were finally rolled together with a stainless steel mesh current collector. The assembly was then dried and sintered for 30 min at 340 °C and 15 MPa and its schematic view was shown in Fig. 1 (a).

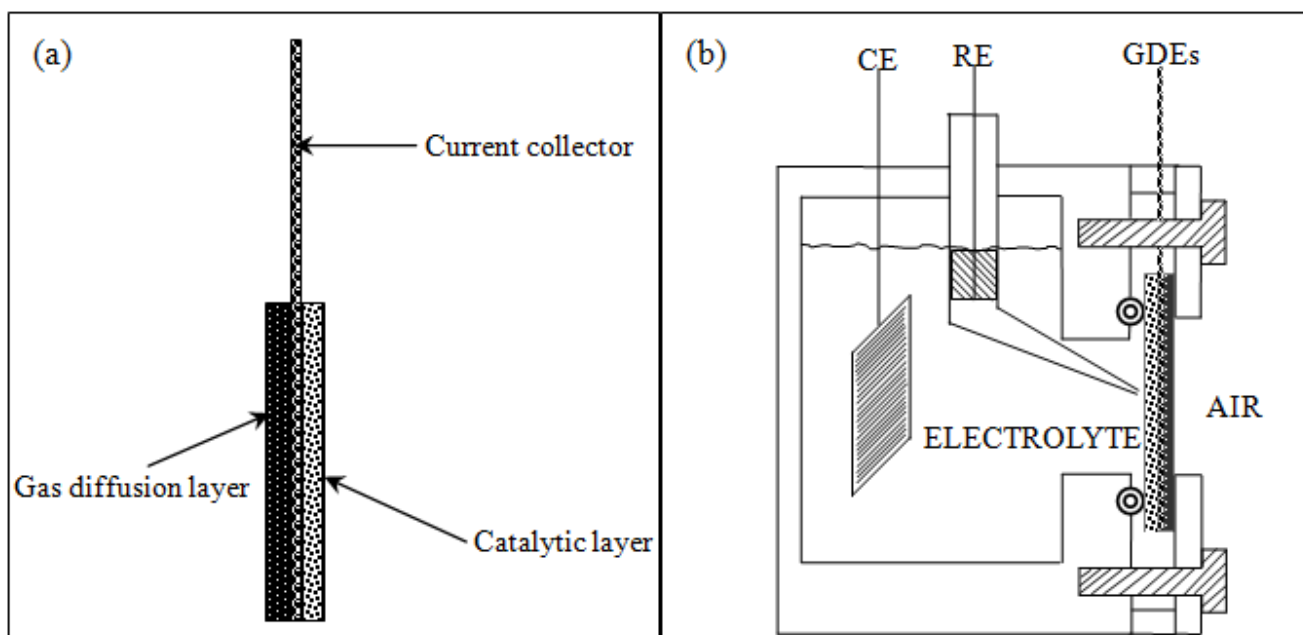


Figure 1. Schematic view of GDEs design (a) and the plexi-glass cell used for electrochemical measurements (b).

The GDEs were characterized with a three-electrode configuration as shown in Fig. 1 (b). An area of 1 cm^2 on the backside of the GDE was exposed to ambient air during measurements. A bright platinum (2 cm^2) foil and an Hg/HgO/ 6 mol L^{-1} KOH electrode were used as counter and reference electrodes, respectively. The electrolyte was 6 mol L^{-1} KOH aqueous solution under air atmosphere and maintained at $25 \text{ }^\circ\text{C}$. The half-cell had been rested for 48 h to assure that the electrolyte had sufficient time to penetrate into the structure of the active layer. In order to obtain steady polarization curves, galvanostatic measurements were applied. Then all polarization curves were obtained until they were repeatable. Electrochemical performances were conducted by Parstat 2273. The i - V polarization curves were obtained under a scan rate of 0.5 mV s^{-1} . Galvanostatic profiles were measured at current densities of 50 and 100 mA cm^{-2} for 10 min. For EIS measurement, the applied frequency range was from 0.01 Hz to 100 kHz with signal amplitude of 5 mV. The overall impedance data was fitted by a complex non-linear least squares fitting program in Z-view 2.0 software. None of the potential measurements in this study were compensated for IR-drops. In the lifetime determination, the GDEs experienced repeating sequences of oxygen reduction (0.5 h), resting (1 h), oxygen evolution (0.5 h), and resting (1 h) at 50 mA cm^{-2} .

3. RESULTS AND DISCUSSION

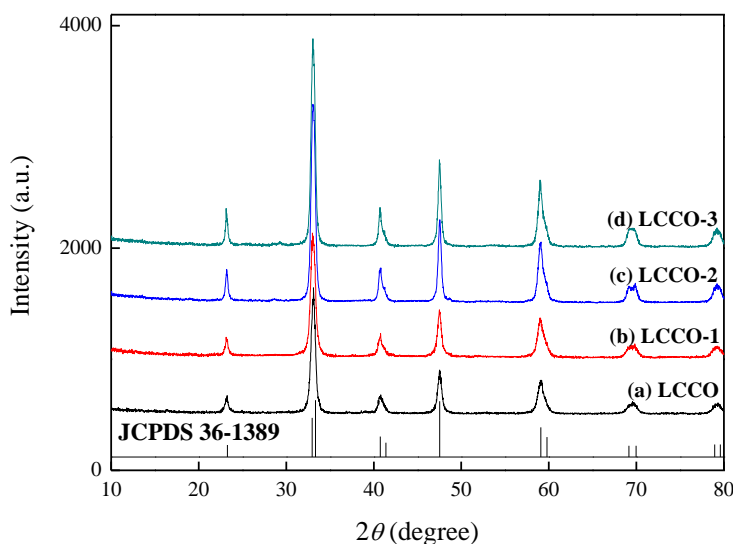


Figure 2. XRD patterns of (b) LCCO-1, (c) LCCO-2 and (d) LCCO-3 catalysts fired at $650 \text{ }^\circ\text{C}$ together with (a) the ACP-derived LCCO for comparison.

Fig. 2 presents the XRD patterns of the optimization catalysts fired at $650 \text{ }^\circ\text{C}$ and the ACP-derived LCCO for comparison. The XRD result of the ACP-derived powders exhibited a pure perovskite $\text{La}_{0.6}\text{Ca}_{0.4}\text{CoO}_3$ phase, without any unwanted oxides, which agreed perfectly with the JCPDS standard data (36–1389). For the nonporous samples, they also presented the typical pattern of

perovskite $\text{La}_{0.6}\text{Ca}_{0.4}\text{CoO}_3$ and no other impurities were detected from the XRD patterns. The relative intensity of the diffraction peaks of $\text{La}_{0.6}\text{Ca}_{0.4}\text{CoO}_3$ strengthened with the content of pore-forming material increasing. This might be ascribed to the more pore-forming materials releasing the more heat, which were beneficial to formation of perovskite $\text{La}_{0.6}\text{Ca}_{0.4}\text{CoO}_3$ at the same calcination temperature. And the average crystalline size of the calcined samples at 650 °C was calculated based on the Scherrer equation [32] and the size was between 34 and 40 nm.

Fig. 3(a)-(d) shows the morphologies of the as-synthesized powders calcined at 650 °C, together with the EDS spectrum of the particles in the selected regions. There were no obvious differences in the EDS spectrum of the two samples. EDS detected trace amount of the carbon element in the both samples, which might come from the carbon tap during the EDS test.

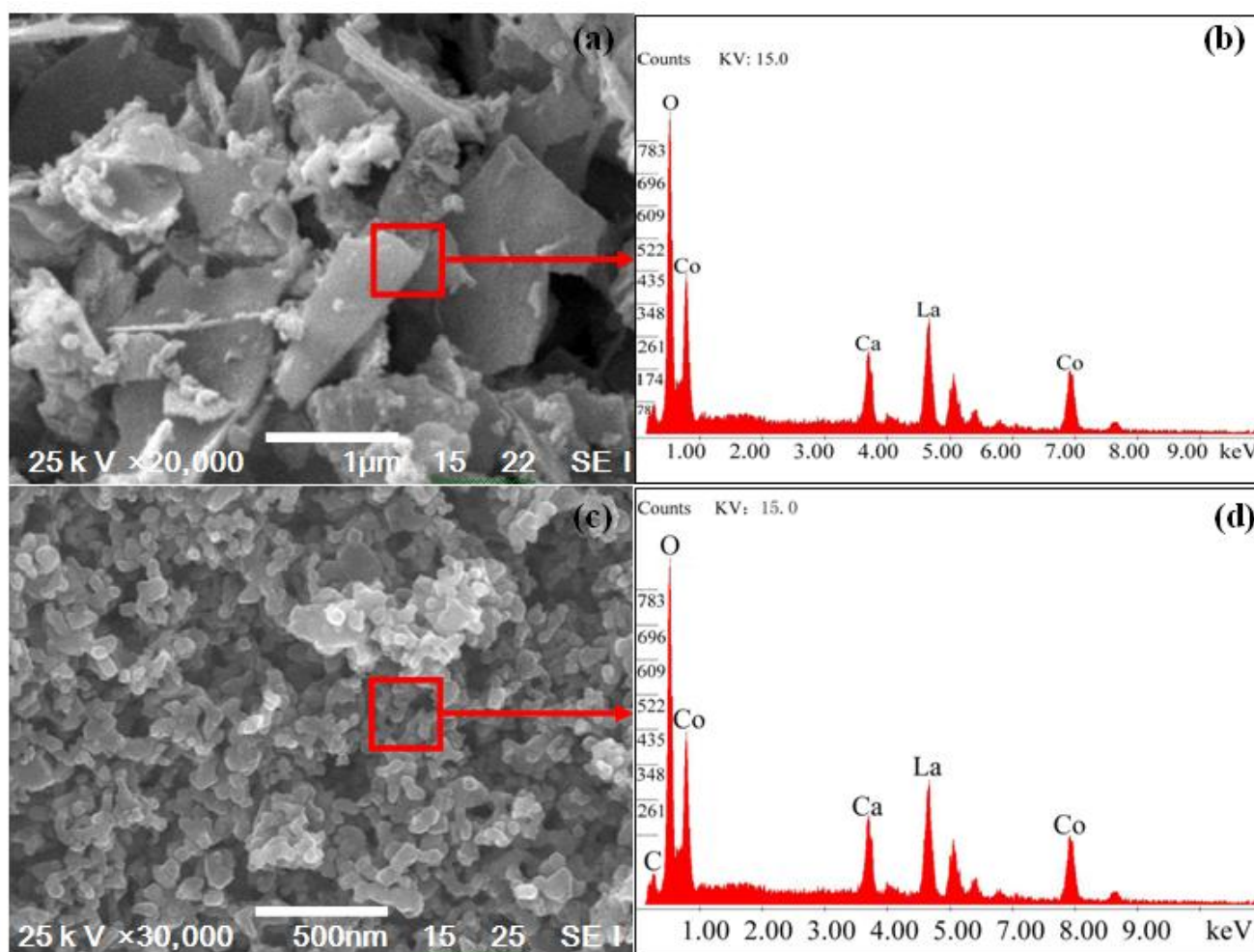


Figure 3. SEM images of the ACP-derived $\text{La}_{0.6}\text{Ca}_{0.4}\text{CoO}_3$ powders (a) and the LCCO-3 (b) together with the EDS spectra collected onto the square zones of images (c) and (d) for comparison.

As shown in Fig. 3 (a) and (c), the ACP-derived LCCO powder was irregular morphology with an average particle size of over 1 μm. Due to the pore-forming material introduction, the LCCO-3

presented a novel nanoporous structure and the particle size was around 50 nm, which was consistent with the XRD results.

Table 1. The specific surface area of the as-synthesized catalysts.

Samples	LCCO	LCCO-1	LCCO-2	LCCO-3
Specific surface area (m ² /g)	43	86	120	210

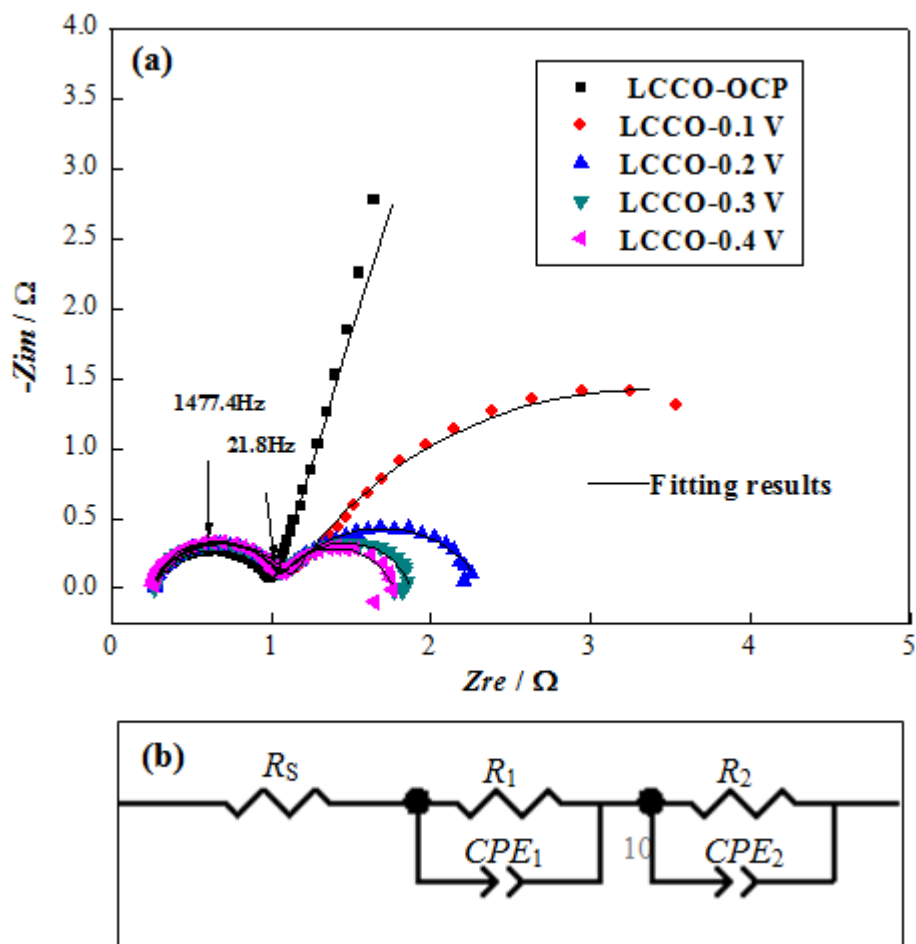


Figure 4. Impedance spectra of the GDEs catalyzed by the ACP-derived LCCO recorded at cathodic potentials of -100, -200, -300, -400 mV (vs. OCP) and the fitting results (a); schematic representation of the equivalent circuit for the EIS of the bifunctional air electrode (b).

The nanoporous morphology of the as-prepared samples would provide much convenience for the electrolyte and oxygen diffusing into the catalyst powders [33]. The specific surface areas of these as-synthesized powders determined by the BET technique were listed in table 1. It was obvious to find

that the specific surface areas of $\text{La}_{0.6}\text{Ca}_{0.4}\text{CoO}_3$ increased significantly with the content of pore-forming material increasing. It was because that the carbon can not only hinder the growth of solid particles during heating [34] but also act as the pore-forming material after burning out which causes nanoporous structure forming. Such a high specific surface area supplies a number of surface active sites, which facilitate the material's electrocatalytic properties.

To understand the reaction processes of GDEs, the EIS characteristic of the electrode catalyzed by the ACP-derived LCCO has been investigated. The corresponding Nyquist plots at the different cathodic potentials and the fitting results are shown in Fig. 4 (a). Two semi-circles were observed in the frequency range from 100 kHz to 100 mHz. The Nyquist plots displayed a high frequency potential-independent loop and a low frequency potential-dependent loop as described in reference [29]. The spectra were fitted with an equivalent circuit shown in Fig. 4 (b). The resistance R_s represented the sum of electrolyte resistance and contact resistances. It was the high frequency intercept with the real axis in the Nyquist plot. The two semi-circles were described by a series of two parallel RC elements, whereby the capacitances were replaced by constant phase elements. CPE_1 and CPE_2 represented the double-layer capacitance distributed between the ohmic and Faradic processes. The high frequency resistance R_1 accounted for electrode intrinsic resistance (distributed resistances inside the porous structure) and the low frequency resistance R_2 was related to kinetic impedance of ORR (charge transfer processes at the catalyst surface in a part and reacting species diffusion through the thin film in another part) [27].

In the GDEs system, the charge-transfer term is usually affected by the reaction temperature, and the diffusion term is influenced by convection. In order to confirm the validity of the equivalent circuit for this GDEs system, the EIS tests of the electrode were performed under various temperatures and different air flow conditions, respectively.

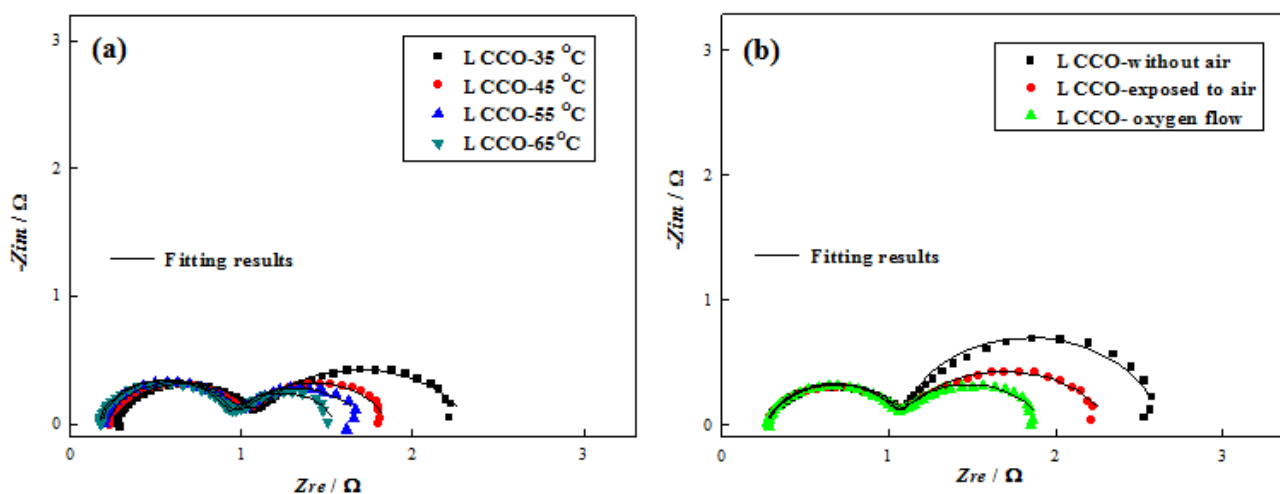


Figure 5. Impedance spectra of the ACP-derived LCCO electrode recorded at cathodic potentials of -0.2 (vs. OCP) at 35 °C, 45 °C, 55 °C, 65 °C and the fitting results (a); under without air, exposed to air, with oxygen flow at room temperature and the fitting results (b).

Their spectra and the fitting results were presented in Fig. 5. As shown in Fig. 5 (a), R_s was decreased slightly with the increasing temperature due to the decrease of the electrolyte resistance [28]. The size of the first loop at the high frequency remained virtually unchanged when the temperature changed. But, the size of the second one at the low frequency decreased with increasing the temperature. As shown in Fig. 5 (b), the size of the first loop at the high frequency kept almost constant when the air supply condition was changed. While, the size of the second loop at the low frequency decreased with increasing the oxygen concentration. Therefore, the first loop at the high frequency was independent on the reaction temperatures and the air supply condition while the second one was dependent on these two factors. Hence, the stable size of the first one in the high frequency region was ascribed to distributed resistances inside the porous structure. The second one, which was expected for kinetic impedance of ORR, decreased with the increasing overpotentials, reaction temperatures and convection. And the results of EIS can be fitted well by the equivalent circuit, further confirming that this equivalent circuit for the GDEs system was reasonable.

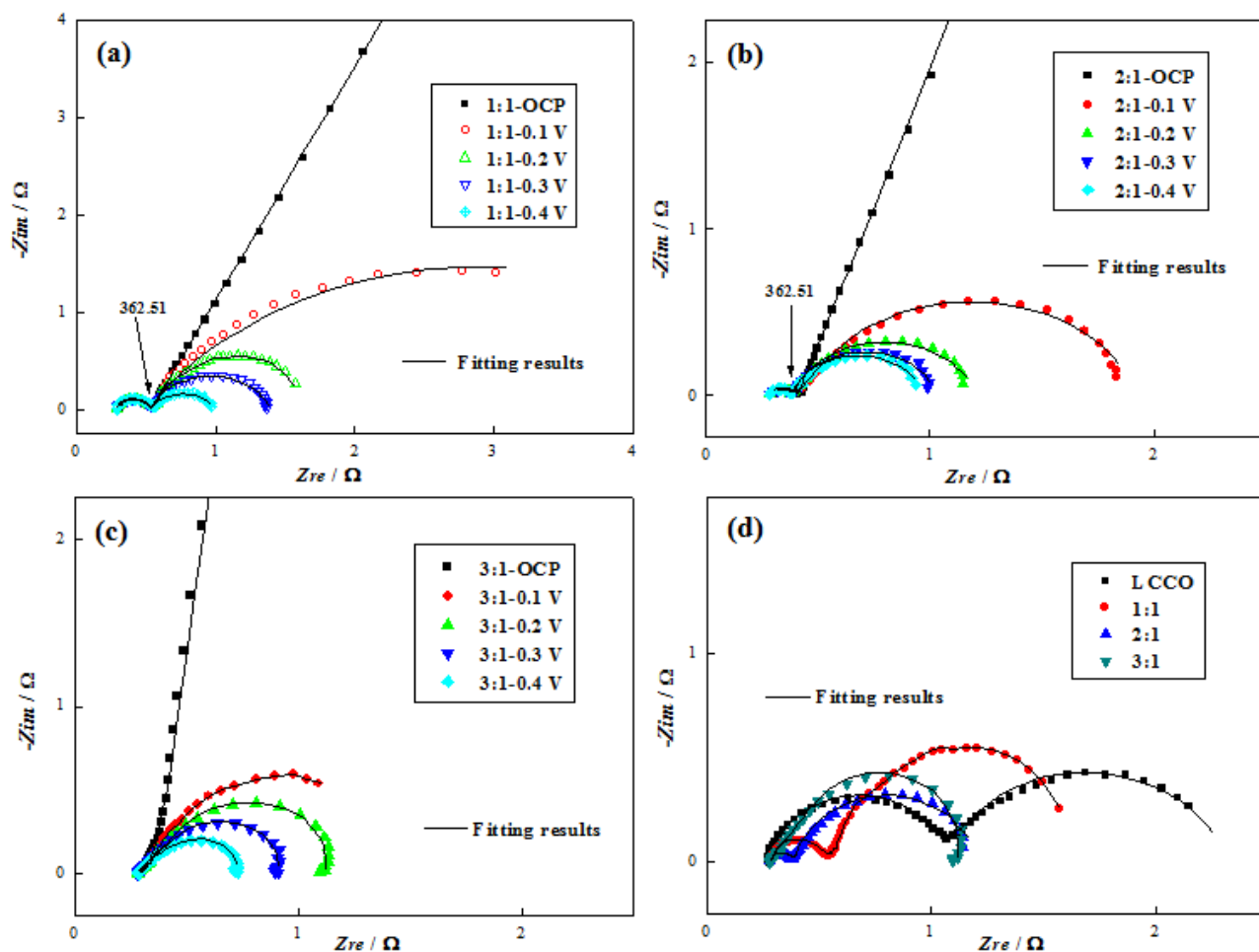


Figure 6. Impedance spectra of the GDEs catalyzed by LCCO-1 (a), LCCO-2 (b) and LCCO-3 (c) recorded at cathodic potentials of -100, -200, -300, -400 mV (vs. OCP), the ACP-derived LCCO and nanoporous LCCO catalysts electrodes at a potential of -200 mV (d) together with the fitting results.

For investigating the improvement of the nanoporous structural catalysts on the electrochemical performance of GDEs, the EIS tests of the LCCO-1, LCCO-2 and LCCO-3 electrodes at different cathodic potentials were performed and the above equivalent circuit (Fig. 4 (b)) was matched with the results. As shown in Fig. 6 (a)-(c), the size of the first loop at the high frequency kept almost constant, but the second one at the low frequency decreased obviously with the overpotential increasing for each samples, which were similar to the ACP-derived LCCO case. For these three samples, the size of the first loop at the high frequency decreased obviously and then disappeared finally with the pore-forming material increasing, indicating that the intrinsic resistance of GDEs can be reduced when the interconnected pore of $\text{La}_{0.6}\text{Ca}_{0.4}\text{CoO}_3$ catalyst form channels for the electrolyte and air to move into the catalyst powders. Due to the submicron radius of these channels, the capillary force would be strong enough to hold the electrolyte and prevent it from over flooding the electrode.

In order to confirm the effect of the nanoporous $\text{La}_{0.6}\text{Ca}_{0.4}\text{CoO}_3$ on their catalytic activity in the GDEs, the Nyquist plots of the electrodes with these optimized catalysts for ORR obtained at potentials of -200 mV (vs. OCP) are shown in Fig. 6(d) and the plots were fitted with aforesaid equivalent circuit (Fig. 4(b)). The parameters were obtained from the data in Fig. 6(d) and listed in Table 2. R_1 decreased gradually with the increasing content of the pore-forming material, providing further evidence that the nanoporous catalyst decrease the intrinsic impedance of GDEs. Furthermore, R_2 also became smaller when the content of the pore-forming material was higher, illustrating that the nanoporous $\text{La}_{0.6}\text{Ca}_{0.4}\text{CoO}_3$ can also decrease the kinetic impedance of GDEs. Generally, the smaller the particle size of the catalyst is, the higher the utilization efficiency and the catalytic activity for ORR are. This increased activity might be explained by nanoporous $\text{La}_{0.6}\text{Ca}_{0.4}\text{CoO}_3$ catalyst providing higher internal specific surface area and large number of surface sites.

Table 2. The corresponding fitting parameters of Fig. 6(d) for ORR on GDEs

Composition of catalyst	R_s / Ω	R_1 / Ω	CPE_{1-T} / F	CPE_{1-P}	R_2 / Ω	CPE_{2-T} / F	CPE_{2-P}
$\text{La}_{0.6}\text{Ca}_{0.4}\text{CoO}_3$	0.27	0.84	6.7×10^{-4}	0.84	1.26	0.15	0.75
LCC-1	0.28	0.236	1.36×10^{-4}	0.94	1.18	0.27	0.68
LCC-2	0.28	0.12	2.2×10^{-3}	0.73	0.82	0.091	0.83
LCC-3	0.28	0.08	0.18	0.71	0.56	0.081	0.93

In order to gain additional information on ORR, the polarization performance of these electrodes has been investigated and the corresponding polarization curves are shown in Fig. 7. Among these polarization curves, the optimizing catalysts prepared by the modified-ACP method all presented higher catalytic ability for ORR and OER than the ACP-derived LCCO. The electrode catalyzed by LCCO-3 exhibited the smallest polarization delivering -0.163 mV at 100 mA cm^{-2} and 0.692 (vs. Hg/HgO) at 50 mA cm^{-2} , respectively. It was further confirmed that more rapid oxygen adsorption and desorption occurred when the nanoporous LCCO-3 was used as catalyst, which had the largest specific surface area and provided more available active sites for ORR and OER.

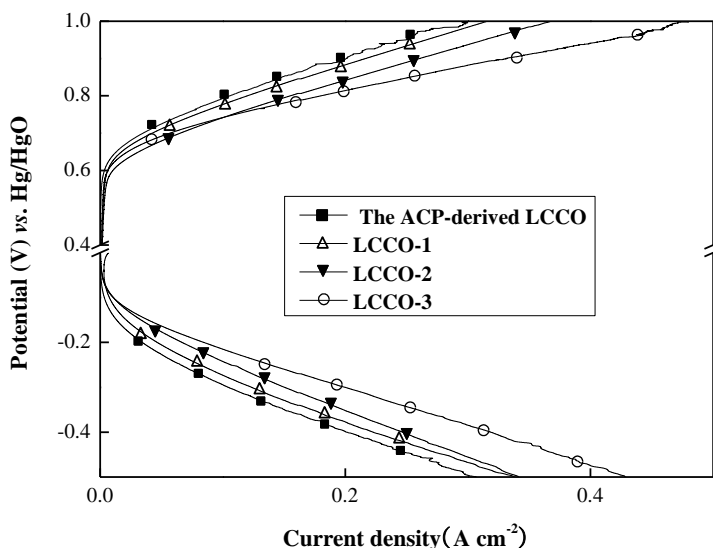


Figure 7. Anodic and cathodic polarization curves of the GDEs catalyzed by the ACP-derived LCCO, LCCO-0.03Ag and LCCO-3, respectively.

To fairly compare the bi-functional ability and the stability of LCCO-3 with those of the ACP-derived LCCO, the electrodes were subjected to 100 cycles of oxygen reduction and evolution under the current density at 50 mA cm^{-2} . The results are shown in Fig. 8, as for the two samples, the potential readings presented here were in accordance with the results of *i-V* polarization curves.

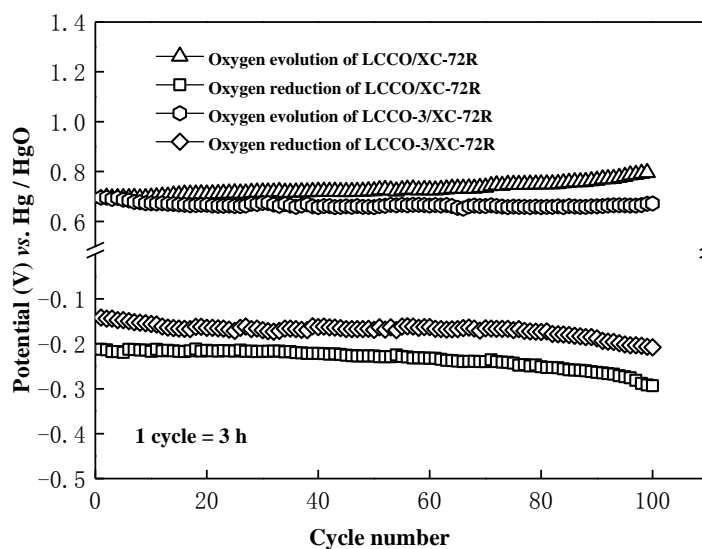


Figure 8. The cycle life performance of LCCO-3/XC-72R-catalyzed GDE and the ACP-derived $\text{La}_{0.6}\text{Ca}_{0.4}\text{CoO}_3/\text{XC-72R}$ -catalyzed GDE for comparison with the current density at 50 mA cm^{-2} .

The voltage plateaus were rather flat, indicating that the catalytic performances of LCCO-3 were stable and sustainable in alkaline electrolyte. In addition, the electrocatalytic performance of LCCO-3 was consistently higher than those of LCCO when charging and discharging. This effectively

demonstrated that the well-dispersed nanoporous LCCO-3 as the bi-functional catalyst led to a significant improvement in the electrochemical performance of the half-cell.

4. CONCLUSIONS

The homogeneous nanoporous $\text{La}_{0.6}\text{Ca}_{0.4}\text{CoO}_3$ catalysts were prepared by a modified amorphous citrate precursor method. Based on XRD and EDS results, the optimizing samples presented pure perovskite phases and were all well crystallized at 650 °C. It was observed that the addition of the pore-forming material significantly influenced their microstructure and catalytic activity. The EIS analysis indicated that the nanoporous $\text{La}_{0.6}\text{Ca}_{0.4}\text{CoO}_3$ not only reduced the intrinsic impedance, but also increased the ORR kinetics of GDEs, which was because the interconnected pore of the nanoporous catalyst forming channels were convenient for the electrolyte and air to move into the catalyst powders, and the larger surface area was more available for evolution and reduction of oxygen. In *i-V* polarization characterizations, the LCCO-3 exhibited better performance than those of the ACP-derived LCCO under both charge and discharge modes. Results from the cycle life tests indicated that the electrocatalytic abilities of LCCO-3 were stable and sustainable for possible application in metal-air batteries and low-power fuel cells.

ACKNOWLEDGEMENTS

This work was financially supported by Talents Introduction Program of Xiamen University of Technology (No. YKJ12019R) and JK Program of Fujian Province (No. JK2013034).

References

1. E. Deiss, F. Holzer, O. Haas, *Electrochim Acta*, 47 (2002) 3995
2. C.C. Yang, S.J. Lin, *J. Power. Sources.*, 112 (2002) 497
3. A.A. Mohamad, *J. Power. Sources.*, 159 (2006) 752
4. C.W. Lee, K. Sathiyarayanan, S.W. Eoma, H.S. Kima, M.S. Yun, *J. Power. Sources.*, 159 (2006) 1474
5. M.N. Masri, A.A. Mohamad, *Corros. Sci.*, 51 (2009) 3025
6. G.M. Wu, S.J. Lin, C.C. Yang, *J. Membr. Sci.*, 280 (2006) 802
7. C.W. Lee, K. Sathiyarayanan, S.W. Eoma, H.S. Kima, M.S. Yun, *J. Power. Sources.*, 160 (2006) 1436
8. X. Wang, P.J. Sebastian, M.A. Smit, H. Yang, S.A. Gamboab, *J. Power. Sources.*, 124 (2003) 278
9. H. Falcón, R.E. Carbonio, *J. Electroanal. Chem.*, 339 (1992) 69
10. R.E. Carbonio, C. Fierro, D. Tryk, D. Scherson, E. Yeager, *J. Power. Sources.*, 22 (1988) 387
11. M. Pirjamali, Y. Kiros, *J. Power. Sources.*, 109 (2002) 446
12. M. Bursell, M. Pirjamali, Y. Kiros, *Electrochim. Acta.*, 47 (2002) 1651
13. V. Neburchilov, H.J. Wang, J.J. Martin, W. Qu, *J. Power. Sources.*, 195 (2010) 1271
14. C. Davidson, G. Kissel, S. Srinivasan, *J. Electroanal. Chem.*, 132 (1982) 129
15. F. Svegli, B. Orel, I. Grabec-Svegli, V. Kaucic, *Electrochim. Acta.*, 45 (2000) 4359
16. A.K. Shukla, A.M. Kannan, M.S. Hegde, J. Gopalakrishnan, *J. Power. Sources.*, 35 (1991) 163
17. J. Prakash, D.A. Tryk, W. Aldred, E.B. Yeager, *J. Appl. Electrochem.*, 29 (1999) 1463
18. N.L. Wu, W.R. Liu, S.J. Su, *Electrochim. Acta.*, 48 (2003) 1567

19. D. Chartouni, N. Kuriyama, T. Kiyobayashi, J. Chen, *J. Alloys. Compd.*, 330-332 (2002) 766
20. N.A. Merino, B.P. Barbero, P. Eloy, L.E. Cadús, *Appl. Surf. Sci.*, 253 (2006) 1489
21. A. Kahoul, A. Hammouche, G. Poillerat, R.W. De Doncker, *Catal. Today.*, 89 (2004) 287
22. V. Hermann, D. Dutriat, S. Müller, C. Comninellis, *Electrochim. Acta.*, 46 (2000)365
23. E. Yeager, *Electrochim. Acta.*, 29 (1984) 1527
24. Y.M. Chang, P.W. Wu, C.Y. Wu, *Electrochem. Solid. State. Lett.*, 11 (2008) B47
25. Y.M. Chang, Y.C. Hsien, P.W. Wu, C.H. Lai, T.Y. Chang, *Mater. Lett.*, 62 (2008) 4220
26. Y.M. Chang, P.W. Wu, C.Y. Wu, Y.C. Hsien, *J. Power. Sources.*, 189 (2009) 1003
27. S. Zhuang, K. Huang, C. Huang, H. Huang, S. Liu, M. Fan, *J. Power. Sources.*, 196 (2011) 4019
28. D. Thiele, A. Züttel, *J. Power. Sources.*, 183 (2008) 590
29. H. Huang, W. Zhang, M. Li, Y. Gan, J. Chen, Y. Kuang, *J. Colloid. Interface. Sci.*, 284 (2005) 593
30. H. Arai, S. Müller, O. Haas, *J. Electrochem. Soc.*, 147 (2000) 3584
31. S. Zhuang, C. Huang, K. Huang, X. Hu, F. Tu, H. Huang, *Electrochem. Commun.*, 13 (2011) 321
32. M. Gaudon, C. Laberty-Robert, F. Ansart, L. Dessemond, P. Stevens, *J. Power. Sources.*, 133 (2004) 214
33. J. Yang, J.J. Xu, *Electrochem. Commun.*, 5 (2003) 306
34. H.P. Liu, Z.X. Wang, X.H. Li, H.J. Guo, W.J. Peng, Y.H. Zhang, Q.Y. Hu, *J. Power. Sources.*, 184 (2008) 469